Catalysis Science & Technology

PAPER

View Article Online
View Journal | View Issue

Cite this: *Catal. Sci. Technol.*, 2018, **8**, 2966

Synthesis of high-Si hierarchical beta zeolites without mesoporogen and their catalytic application in the methanol to propene reaction†

Xuebin Zhao,[abc] Linying Wang,[a] Peng Guo,[a] Nana Yan,[ab] Tantan Sun,[ab] Shanfan Lin,[ab] Xinwen Guo,[c] Peng Tian*[a] and Zhongmin Liu*[a]

Received 28th March 2018,
Accepted 8th May 2018

DOI: 10.1039/c8cy00631h

rsc.li/catalysis

High-Si single-crystalline beta zeolites with intracrystal mesopores were synthesized for the first time and investigated as catalysts for the methanol to propene (MTP) reaction. A fast and mesoporogen-free strategy was developed to fabricate the hierarchical structures by conducting crystallization under low water conditions (H_2O/SiO_2 = 1). Low water dosage for the synthesis was demonstrated to facilitate the nucleation and crystal growth, but restrained the fusion of individual nanocrystallites inside the particles, which helped the formation of hierarchical structures. The resultant hierarchical beta with Si/Al = 277 exhibited a much longer catalytic lifetime and slower coking rate than conventional zeolite due to the improved utilization of interior acid sites and enhanced molecular diffusion. A higher propene selectivity (50.2–55.5%) and propene/ethene ratio were also found for the hierarchical sample, which can be ascribed to the reduced side reactions of olefin products. The methanol conversion mechanism over the high-Si hierarchical beta was investigated by $^{12}C/^{13}C$-methanol isotopic labeling experiments, which revealed the predominant route of the olefin methylation and cracking mechanism for the formation of olefins.

1. Introduction

Zeolites have been widely used as shape-selective catalysts in the petrochemical and fine chemical industries.[1] However, reactant and product diffusion limitations imposed by the microporous nature of zeolites may restrict their catalytic performance, leading to low utilization of active sites and poor catalytic activity. The problem can be overcome by reducing the diffusion path in the zeolites through decreasing the size of zeolite crystals or constructing mesopores in zeolite crystals.[2,3] Among the solutions, direct synthesis of mesoporous zeolites has attracted considerable attention[4–7] because it can circumvent the separation problem of nanozeolites and allows better control of mesopore sizes and zeolite structure integrity as compared to post-treatment methods.[8–13]

Hitherto, various strategies have been developed to synthesize hierarchical structures, which can be mainly classified as hard-templating[14,15] and soft-templating routes.[16,17] The hard-templating method, which was first employed for the synthesis of mesoporous zeolites, usually consumes a large amount of hard substrates and is unfavorable for industrial production. On the other hand, great progress has been made during the past decade by using soft templates such as polymers, surfactants or well-designed bifunctional surfactants containing micropore directing multi-ammonium heads and mesopore directing alkyl tails.[16,18–22] A number of hierarchical zeolites with tunable mesoporosity have been achieved by a soft-templating approach. In addition, to effectively avoid the introduction of secondary templates, simplify the synthesis procedure and reduce the synthetic cost, non-template methods in which crystal growth and assembly are carefully regulated to yield hierarchical structures have to be developed. However, successful examples of the non-template route are relatively rare and no general strategy has currently been proposed due to the complexity of the zeolite crystallization system and the lack of modulation means.

Zeolite beta, with a three-dimensional interconnected pore system composed of 12-memberbed rings, is one of the most important zeolites that achieved industrial application.[23–25] The syntheses of hierarchical beta with improved catalytic properties have been achieved *via* hard-templating, soft-templating and non-templating approaches.[26–29] However,

[a] *National Engineering Laboratory for Methanol to Olefins, Dalian National Laboratory for Clean Energy, Dalian Institute of Chemical Physics, Chinese Academy of Sciences, Dalian 116023, P.R. China. E-mail: tianpeng@dicp.ac.cn, liuzm@dicp.ac.cn; Fax: +86 411 84379289; Tel: +86 411 84379998*
[b] *University of Chinese Academy of Sciences, Beijing 100049, P. R. China*
[c] *State Key Laboratory of Fine Chemicals, PSU-DUT Joint Center for Energy Research, School of Chemical Engineering, Dalian University of Technology, Dalian 116024, P.R. China*

† Electronic supplementary information (ESI) available: More details of the experiment, additional XRD patterns, SEM, ^{27}Al MAS NMR, NH_3-TPD and porous properties of samples. See DOI: 10.1039/c8cy00631h

the Si/Al ratios of the reported hierarchical beta were all limited to be less than 50. This is likely due to the difficulty in synthesizing high/pure Si beta, which generally needs the assistance of F^-. In addition, perfect micrometer-sized crystals were easily gained due to the lower super-saturation and nucleation rates caused by the weaker mineralizing power of F^-.[30]

The methanol to olefin reaction, which provides an alternative route for the production of light olefins from non-oil resources, has drawn considerable attention in both academia and industry. It is generally accepted that the reaction on zeolite catalysts follows an indirect pathway in which two catalytic cycles may be involved, that is, an aromatic-based cycle and an olefin-based cycle.[31] In the aromatic-based cycle, methylbenzenes, methylcyclopentadienes and their corresponding carbenium cations are revealed to be the active hydrocarbon pool species, which favors the production of ethene and propene; in the olefin-based cycle, higher olefins formed by the methylation of light olefins are reactive intermediates, which crack and mainly contribute to the production of propene and butene. It is mentioned that the relative ratio of the two cycles can be tuned by altering the zeolite topology, acidity and reaction conditions, and thus the product selectivity can be adjusted.[32–38]

The catalyst development for the methanol to olefin process is mainly focused on small-pore (*e.g.* SAPO-34) and medium-pore (*e.g.* ZSM-5) zeolites based on the consideration of shape-selectivity control. Large-pore zeolites receive less attention due to the lack of space limitation and the studies based on them mainly aim to clarify the reaction mechanisms. Previous studies about methanol conversion over large-pore beta were focused on zeolites with low Si/Al ratios, which gave a large amount of aromatic products due to the high acid concentration of the catalysts.[39–41] The reaction temperature was generally controlled to be about 350 °C for better examination of the reaction mechanism.[40–42] The aromatic-based HCP mechanism was revealed to predominantly contribute to the reaction.[35] Recently, Yokoi *et al.*[43] have developed a post-synthetic dealumination method to improve the Si/Al ratio of beta zeolites and achieved 37.4–49.7% propene selectivity over a dealuminated sample (Si/Al = 112). We[44] also synthesized a series of beta zeolites (Si/Al = 136 to 340) and demonstrated that beta zeolite with Si/Al = 280 possessed the best catalytic performance with high propene selectivity under an optimized reaction temperature of 500–550 °C. It was revealed that the lower acid concentration inhibited the formation of aromatics and the higher reaction temperature facilitated the cracking and diffusion of heavy products, both of which worked together and contributed to the improved catalytic performance. Moreover, Liu *et al.*[40] reported that hierarchical beta zeolite with a Si/Al ratio of about 30 exhibited a 2.7-fold larger conversion capacity and a longer lifetime than conventional beta zeolite at 330 °C. The hierarchical structure disfavored the propagation of an aromatic-based cycle due to the shortened residence time of methylbenzenes in zeolite micropores, leading to a higher selectivity to higher aliphatics (C_4–C_7). This suggests that the enhancement of mass transfer promoted by hierarchical pore systems can alter product distribution and facilitate longer lifetimes. It is thus envisioned that high-Si beta with hierarchical structures may present a more interesting catalytic performance in the methanol conversion reaction.

In this contribution, high/pure silica hierarchical beta zeolites were synthesized for the first time, which was achieved in a fluorine medium under extremely low water conditions without the assistance of a mesoporogen. The resulting high-Si hierarchical beta particles were demonstrated to have a single-crystalline nature. The catalytic performance of high-Si hierarchical beta for the methanol conversion was investigated and compared with that of conventional high-Si beta zeolite. The reaction mechanism over high-Si hierarchical beta was further investigated by the $^{12}C/^{13}C$ methanol switch technique.

2. Experimental

2.1 Synthesis of beta zeolites

Beta zeolites were synthesized with a molar composition of $1SiO_2 : 1/600Al_2O_3 : 0.5TEAOH : 0.45HF : 1H_2O$, where tetraethoxysilane (TEOS, Tianjin Kemiou Chemical Reagent Co) was used as a silica source, and $Al(NO_3)_3{\cdot}9H_2O$ (Tianjin Kemiou Chemical Reagent Co) acted as an aluminium source. Typically, 31.56 g of 35 wt% tetraethylammonium hydroxide (TEAOH) solution (Tianjin Jingrun Chemical Co) was added to 31.25 g TEOS under stirring. After 2 h, 0.188 g $Al(NO_3)_3{\cdot}9H_2O$ dissolved in 4.0 g water was mixed with the above clear solution and further stirred for 0.5 h, followed by the fast addition of 3.4 g of 40 wt% HF solution (Tianjin Damao Chemical Co). The redundant water was evaporated at 60 °C to obtain the final gel. The gel reacted at 160 °C for 8 h with tumbling at 60 rpm within a Teflon-lined stainless steel autoclave. The resultant slurry was centrifuged, washed with distilled water three times, dried at 120 °C for 12 h, and further calcined at 550 °C for 4 h to remove the organic template in the products. The solid yield of the products was calculated on a SiO_2 basis. The sample was named B*x*-*y*, where *x* represents the Si/Al ratio in the gel and *y* refers to the H_2O/SiO_2 ratio.

2.2 Characterization

The powder XRD pattern was recorded on a PANalytical X'Pert PRO X-ray diffractometer with Cu-Kα radiation (λ = 0.15418 nm), operating at 40 kV and 40 mA. The chemical composition of solid samples was determined with a PhilipsMagix-601 X-ray fluorescence (XRF) spectrometer. The crystal morphology was observed using a scanning electron microscope (Hitachi SU8020). N_2 adsorption–desorption isotherms at −196 °C were determined using a Micromeritics ASAP2020. Prior to the measurement, samples were degassed at 350 °C under vacuum for 4 h. The total surface area was calculated based on the BET equation. The micropore volume and micropore surface area were evaluated using the *t*-plot

method. All solid state NMR experiments were performed using a Bruker Avance III 600 spectrometer equipped with a 14.1 T wide-bore magnet. The resonance frequencies in this field strength were 150.9 and 119.2 MHz for ^{27}Al and ^{29}Si, respectively. The ^{29}Si MAS NMR spectrum was recorded at a spinning rate of 8 kHz using high-power proton decoupling. 1024 scans were accumulated with a $\pi/4$ pulse width of 2.5 μs and a 10 s recycle delay. Chemical shifts were referenced to 4,4-dimethyl-4-silapentane sulfonate sodium salt (DSS). ^{27}Al MAS NMR spectra were recorded at a spinning rate of 12 kHz using one pulse sequence. 200 scans were accumulated with a $\pi/8$ pulse width of 0.75 μs and a 2 s recycle delay. Chemical shifts were referenced to $(NH_4)Al(SO_4)_2{\cdot}12H_2O$ at −0.4 ppm. Temperature-programmed desorption of ammonia (NH_3-TPD) was measured on a Micromeritics 2920 chemical adsorption instrument. Each sample (40–60 mesh, 0.20 g) was loaded into a quartz U-shaped reactor and pretreated at 600 °C for 1 h in flowing He. After the pretreatment, the sample was cooled to 100 °C and saturated with NH_3 gas. Then, NH_3-TPD was carried out under a constant flow of He (20 mL min^{-1}) from 100 to 550 °C at a heating rate of 10 °C min^{-1}.

2.3 Catalytic reaction

0.3 g catalyst was pressed, sieved to 40–60 mesh and loaded in a fixed-bed quartz tubular reactor with an inner diameter of 8 mm. Prior to the reaction, the catalyst was activated at 580 °C for 60 min, and then the temperature was adjusted to 550 °C. Methanol was fed by passing the carrier gas (40.0 ml min^{-1}) through a saturator containing methanol at 35 °C, which gave a WHSV of 4.0 h^{-1}. Methanol conversion was performed under atmospheric pressure. The effluent products from the reactor were kept warm at 200 °C and analyzed using an online Agilent 7890A GC equipped with a PONA capillary column (100 m × 0.25 mm × 0.5 μm) and a FID detector. The conversion and selectivity were calculated on a CH_2 basis. Dimethyl ether (DME) was considered as a reactant in the calculation.

The coke content (in percent) of discharged catalysts was calculated by thermogravimetric analysis (TGA) and the loss between 300 °C and 650 °C was used to estimate the coke content. Considering the different amounts of methanol processed on each catalyst, the average coke deposition rate is defined as follows:

$$R_{\text{coke}} = 10C/((1 - C/100) \times T \times M)$$

where R_{coke} (mg g_{cat}^{-1} h^{-1}) is the average coke deposition rate, C (%) is the coke content in discharged catalysts determined by TGA, T (h) is the reaction time, and M (g) is the amount of catalyst.

2.4 ^{12}C/^{13}C-Methanol switch experiments

In the ^{12}C/^{13}C-methanol switch experiments, after the ^{12}C-methanol was fed for 30 min at 550 °C and WSHV = 4.0 h^{-1}, the feeding was stopped and the feeding line was switched to ^{13}C-methanol for a different time. The effluent products from the reactor were kept warm and analyzed using an online gas chromatograph (GC) equipped with a PoraPLOT-Q capillary column, an FID detector and a mass spectrometric detector (Agilent 7890B/5977A). Meanwhile the off-gas was collected by CH_2Cl_2 every 10 s to better detect the aromatic products; for example, for the 30 s data, the off-gas from 25 s to 35 s was collected. The CH_2Cl_2 solutions were analyzed by a GC-MS (Agilent 7890A/5975C MSD) with a HP-5 MS capillary column.

3. Results and discussion

3.1 Synthesis and characterization of hierarchical beta zeolite under the assistance of fluoride

High-Si hierarchical beta zeolite (sample B300-1) was synthesized from a fluoride-containing semi-dry gel with a molar composition of $1SiO_2 : (1/600)Al_2O_3 : 0.5TEAOH : 0.45HF : 1H_2O$ at 160 °C for 8 h. Detailed synthetic conditions and product properties are listed in Table 1 and the corresponding XRD pattern is shown in Fig. 1. It can be seen that sample B300-1 has a typical diffraction pattern of beta zeolite with the coexistence of sharp and broad peaks, characteristic of different polymorphs with stacking disorder. The Si/Al ratio (277) of sample B300-1 is slightly lower than that of the initial gel (300), which is consistent with the high solid yield of 93.3%. The N_2 adsorption–desorption isotherms are given in Fig. 1, which present a typical type IV isotherm with a hysteresis loop in the P/P_0 range of 0.4–0.99, revealing the existence of mesopores. The mesopore size distribution calculated from the adsorption branch indicates that sample B300-1 has mesopores centered at 4–20 nm (inset in Fig. 2).[45] From Table 1, B300-1 possesses an external surface area of 147 m^2 g^{-1} and a mesopore volume of 0.14 cm^3 g^{-1}. The values are clearly higher than those of sample B300-9 synthesized with a higher H_2O/SiO_2 ratio and consistent with the existence of the mesoporous structure.

The SEM image of sample B300-1 is displayed in Fig. 2a, showing a relatively uniform sphere-like morphology with a particle size of about 1 μm. The higher magnification image (Fig. 2b) reveals that the particle surface is rough with a nanocrystal-assembled morphology. In order to learn the inner structure of the particles, sample B300-1 was mechanically crushed and the corresponding SEM images are illustrated in Fig. 2c and d. It can be seen that the inside is made up of nanocrystals of about 20 nm and the mesopores are rooted in the void space of adjacent nanocrystals. Moreover, the selected area electron diffraction (SAED) pattern of the B300-1 particle was measured and is shown in Fig. 2f. Highly discrete diffraction spots can be observed, suggesting the single crystal feature of the particle. This means that the nanocrystals in hierarchical sample B300-1 grow or assemble in an oriented manner. Generally, synthesis under the F^- system tends to yield perfect crystals in a larger size due to the lower mineralizing ability of F^- than OH^-. Herein, the formation of the nanocrystal-assembled morphology of sample B300-1 should be attributed to the extremely low amount of water in the synthesis system.

Table 1 Detailed synthetic conditions and product properties of beta zeolites synthesized with different H_2O/SiO_2 ratios[a]

Sample	HF/SiO_2	t^b (h)	Solid yield (%)	R^c (%)	Si/Al[d]	Surface area[e] ($m^2\ g^{-1}$)			Pore volume[f] ($cm^3\ g^{-1}$)	
						S_{BET}	S_{micro}	S_{ext}	V_{micro}	V_{ext}
B50-1	0.35	8	96.2	103	46	602	420	182	0.21	0.20
B100-1	0.45	8	94.2	111	96	488	360	128	0.19	0.19
B300-1	0.45	8	93.3	100	277	539	392	147	0.19	0.14
B∞-1	0.55	8	88.9	125	2047	495	373	123	0.18	0.13
B300-3	0.45	12	96.7	112	282	471	373	98	0.18	0.10
B300-6	0.45	48	89.6	115	228	477	399	78	0.19	0.06
B300-9	0.45	72	93.3	108	254	447	383	64	0.20	0.05

[a] The molar ratio of the initial gel: $1SiO_2 : xAl_2O_3 : 0.5TEAOH : yHF : zH_2O$. [b] Crystallization time. [c] Relative crystallinity calculated based on the intensity of the characteristic peaks at 7.8° and 22.4°. [d] Determined by XRF. [e] S_{BET}: BET surface area, S_{micro}: *t*-plot microporous surface area, $S_{ext} = S_{BET} - S_{micro}$. [f] V_{micro}: *t*-plot microporous volume, $V_{ext} = V_{total} - V_{micro}$ (V_{total} is evaluated at $P/P_0 = 0.98$).

It is interesting to note that hierarchical beta zeolites with varying Si/Al ratios (50-∞) can be synthesized by employing the present synthetic strategy. The synthetic conditions and product properties of the samples are presented in Table 1 and the XRD patterns are shown in Fig. S1.† All samples present the diffraction pattern of zeolite beta and are achieved with high solid yields. The SEM images (Fig. S2†) indicate that the samples have a nanocrystal-assembled morphology similar to that of sample B300-1. However, the aggregated particles become smaller with the decrease of the Si/Al ratios. This phenomenon was also observed for beta zeolite synthesized in a conventional basic medium[46] and may be due to an increased ratio of the nucleation rate to the crystal growth rate as the Al content increases. The textural properties of the samples were characterized by N_2 physisorption (Fig. S3† and Table 1). All samples display a hysteresis loop in the P/P_0 range of 0.4–0.99 with a mesopore size distribution of between 4 and 20 nm. The external surface area and mesopore volume of the samples are above 123 $m^2\ g^{-1}$ and 0.13 $cm^3\ g^{-1}$, respectively. Low-Si beta (sample B50-1) shows an even larger external surface area and mesopore volume than high-Si samples, which is consistent with the decrease in particle sizes.

3.2 Influence of the H_2O/SiO_2 ratio on the synthesis

Table 1 lists the synthetic results and texture properties of high-Si beta synthesized with different H_2O/SiO_2 ratios. It can be seen that the external surface area and mesopore volume of the samples drop following the increase in the H_2O/SiO_2 ratio in the synthetic gel. Meanwhile, the amount of mesopores in the products also shows a converse trend with the initial H_2O/SiO_2 ratio (inset in Fig. S4†). The mesopores almost vanish when the H_2O/SiO_2 ratio increases to 6. The SEM images in Fig. 3 reveal that the crystal size of sample B300-9 is about 10 μm with a truncated square-bipyramidal morphology and smooth surface. It gradually decreases to about 1 μm for sample B300-1 with a nanocystal-assembled morphology (Fig. 2a). The variation in the crystal morphology is consistent with the change of texture properties of the samples, evidencing the importance of the low H_2O amount for achieving the hierarchical structure.[2,47]

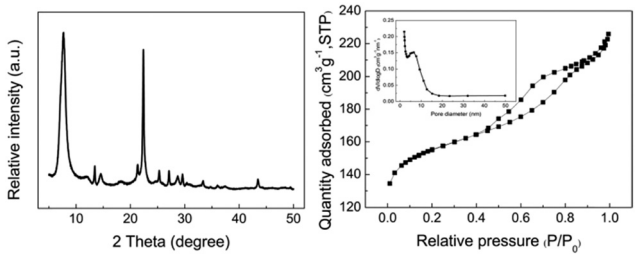

Fig. 1 XRD pattern and N_2 adsorption–desorption isotherms of high-Si beta zeolite (sample B300-1). The inset in the right figure is the pore size distribution curve calculated from the adsorption branch.

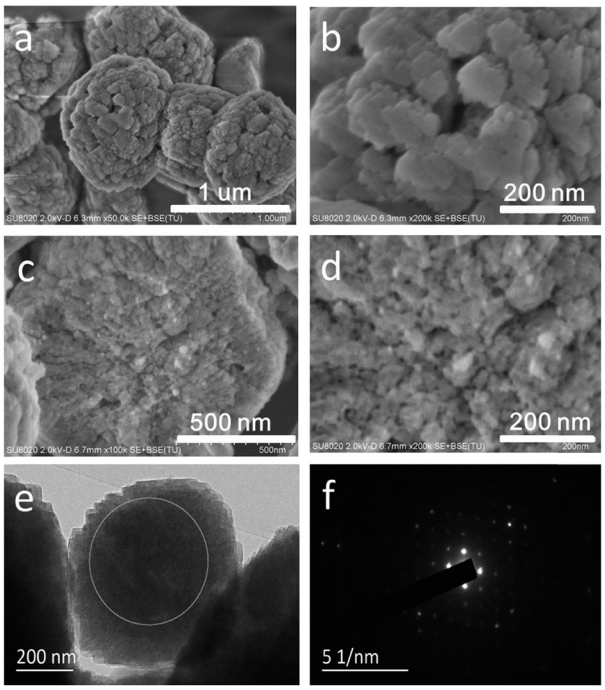

Fig. 2 (a and b) SEM images of sample B300-1; (c and d) SEM images of mechanically crushed B300-1; (e) TEM image of the crushed B300-1 particle; (f) SAED pattern taken with the selected region in (e).

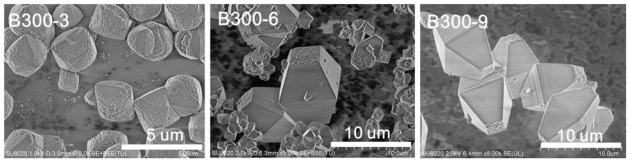

Fig. 3 SEM images of the samples synthesized with different H_2O/SiO_2 ratios.

Fig. 4 displays the crystallization curves of high-Si beta zeolites synthesized with different H_2O/SiO_2 ratios. It is obvious that the induction period is shortened and the growth rate is sharply improved when the H_2O/SiO_2 ratio drops from 6 to 3. On further decreasing the H_2O/SiO_2 ratio to 1, less variation in the crystallization curve is observed, although the external surface area and mesopore volume of the final product show a further increase. These results suggest that the lower H_2O/SiO_2 ratio in the present system not only helps the formation of nanocrystal-assembled morphology but also effectively accelerates the crystallization process.

3.3 The formation of a hierarchical structure in high-Si beta zeolite

In order to understand the formation mechanism of the hierarchical structure of high-Si sample B300-1, an investigation was carried out throughout the duration of the growth process. Table S1† lists the solid yields and product compositions of the samples with different crystallization times. It is clear that the solid yields were maintained at a high level during the whole process and the product compositions show less variation. The photos of the crystallization products before separation and washing are displayed in Fig. S5.† A semi-solid paste can be observed for the incomplete crystallization gels. These findings imply that the mobility of the synthetic components during the crystallization is poor and the products are formed by short range transport of nutrition due to the limited water content.

The N_2 adsorption–desorption isotherms and pore size distribution curves are given in Fig. S6.† Samples crystallized for 2 h possess abundant macropores larger than 20 nm, but they diminish at 4 h and completely vanish at 8 h. At the same time, a mesopore size distribution of between 4 and 20 nm arises for the 8 h well-crystallized product. The surface areas and pore volumes listed in Table S2† indicate that the micropore surface area and micropore volume gradually increase with prolonged crystallization time, whereas the external surface area and pore volume display an opposite trend. Similar phenomena occur for the systems synthesized with H_2O/SiO_2 ratios of 3 and 6 (Table S1†) except for a lower external surface area and fewer mesopores left in the final products.

The SEM images are shown in Fig. 5. For samples heated for 2 h, only small particles of about 20–100 nm can be observed, which connect with each other loosely and leave abundant voids of 20–100 nm. This morphology agrees well with the pore size distribution of the sample (Fig. S6†). After crystallization for 4 h (19.1% relative crystallinity), regular spherical particles of about 500 nm can be observed among the amorphous particles. A higher magnification image (inset in Fig. 5c) reveals that the spherical particles are composed of nanoparticles of about 20 nm. Given that the SAED pattern of the spherical particle (Fig. 5e) gives highly discrete diffraction spots and the corresponding HRTEM image shows clear crystal lattice fringes with consistent orientation (Fig. 5f), it is inferred that the initially formed spherical particles are single-crystalline in nature. With further crystallization for 8 h, the amorphous particles disappear and only nanocrystal-assembled particles in sizes of about 1 μm can be observed (Fig. 2).

Based on the above characterization results, the formation process of hierarchical high-Si beta zeolite is proposed and illustrated in Fig. 6. Porous amorphous particles with macropores and micropores form at the early stage of the crystallization. Afterwards, beta nanocrystallites nucleate from the amorphous particles and form spherical assemblies, which grow larger at the expense of amorphous materials following the progress of the crystallization. The connection of the nanocrystals in the spherical particles is rather loose but in a well-oriented manner, which helps the formation of

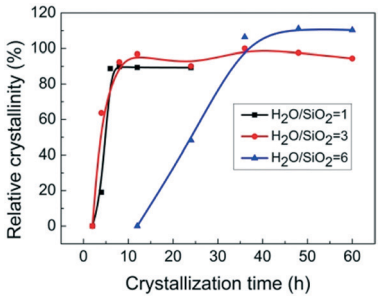

Fig. 4 Crystallization curves of high-Si beta zeolites synthesized with different H_2O/SiO_2 ratios. The initial gel molar composition: $1SiO_2 : 1/600Al_2O_3 : 0.5TEAOH : 0.45HF : mH_2O$ (160 °C).

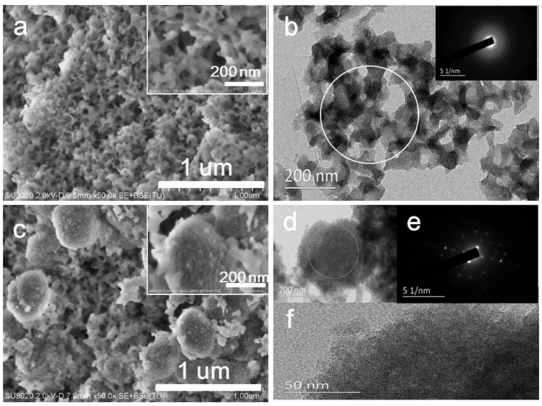

Fig. 5 (a and c) SEM images of the 2 h and 4 h samples, respectively. (b) TEM images and SAED pattern (inset) of the 2 h sample. (d and e) TEM images and SAED pattern (inset) of the 4 h sample. (f) HRTEM image of the 4 h sample.

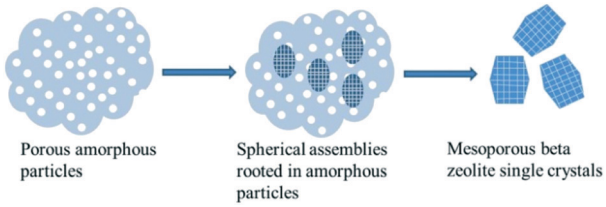

Fig. 6 The formation process of high-silica hierarchical beta zeolite.

mesoporous single-crystalline zeolite. It is mentioned that the growth and fusion of individual nanocrystals inside the particles are restrained possibly due to the low mobility of the components in the synthetic system with such a low H_2O/SiO_2 ratio of 1.

3.4 Acidity and Al distribution in the structure

The acidity and the local atomic coordination environments of high-Si hierarchical sample B300-1 were examined by NH_3-TPD and solid-state MAS NMR, respectively. As a comparison, high-Si beta sample B300-6 synthesized with a higher H_2O/SiO_2 ratio of 6 was also characterized as a reference sample.

The NH_3-TPD curves shown in Fig. 7 present two distinct desorption peaks centered at around 160 and 330 °C, corresponding to the weak and strong acid sites, respectively. The strong acid concentration calculated for hierarchical sample B300-1 is 0.045 mmol g^{-1}, which is slightly lower than that on sample B300-6 (0.053 mmol g^{-1}), possibly due to the lower Si/Al ratio of the latter sample. Note that these values are greatly lower than the acid concentration of sample B50-1 with a Si/Al ratio of 46 (0.23 mmol g^{-1}, Fig. S7†), evidencing the low acid concentration on the high-Si beta samples.

The ^{29}Si and ^{27}Al MAS NMR spectra of the samples are given in Fig. 8. Strong resonance lines at −111.6, −113.0 and −115.7 ppm can be observed, which are ascribed to Si(4Si) species at different crystallographic sites.[48] The ^{27}Al spectra of the samples present two strong overlapping resonances between 50 and 65 ppm arising from tetrahedrally coordinated Al species. In addition, a broad weak resonance ranging from 0 to −20 ppm appears for sample B300-1, which is likely due to the extra-framework octahedral Al in asymmetric and heterogeneous environments.[49,50]

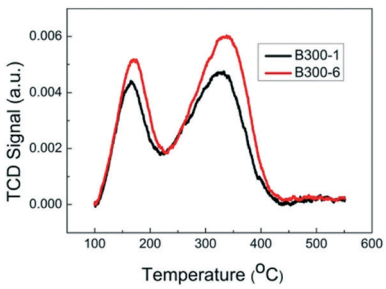

Fig. 7 NH_3-TPD curves of the samples.

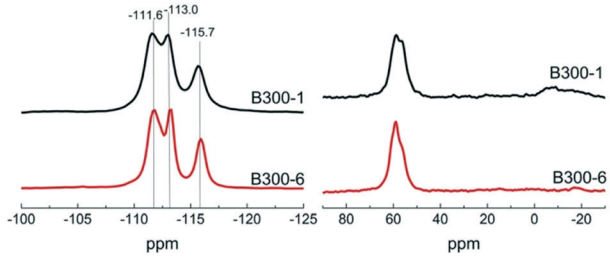

Fig. 8 ^{29}Si (left) and ^{27}Al (right) MAS NMR spectra of the calcined samples.

It has been recognized that the distribution of tetrahedral Al atoms in the zeolite lattices determines their accessibility and affects the acidity and catalytic properties of the zeolites.[51–53] Our previous study[44] also indicated that the Al atoms located at T9 sites in beta zeolite may be favorable Al species for the methanol conversion, which help the catalyst achieve longer catalytic lifetime. Herein, the Al locations at different T sites were determined and the results are displayed in Fig. 9. The detailed fitting process is given in part 1 of the ESI.† From Fig. 9, Al atoms mainly occupy four Al T sites (T3, T7, T8 and T9), despite the existence of nine crystallographically distinct T sites in the beta lattices. Hierarchical sample B300-1 possesses a relatively lower content of the T9 sites in comparison to sample B300-6.

3.5 Methanol conversion over high-Si hierarchical beta zeolite

The combination of a 3D micropore system, mesoporous structure and low acid concentration makes high-Si beta zeolite B300-1 an interesting catalyst for methanol conversion. Herein, catalytic tests of methanol conversion over B300-1

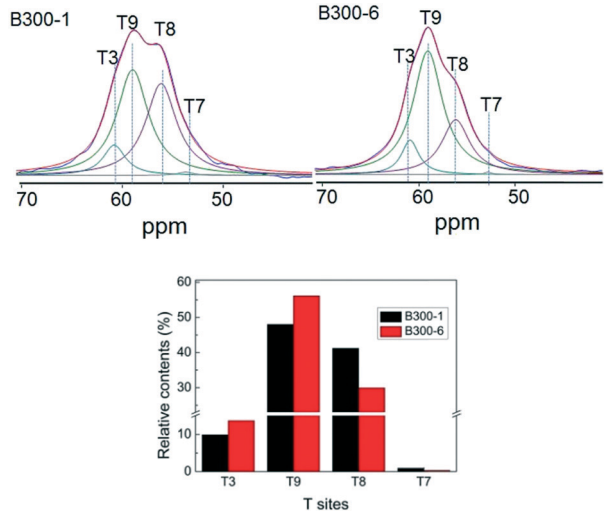

Fig. 9 ^{27}Al MAS NMR spectra with the deconvoluted peaks of tetrahedral Al species and the relative contents of different T sites of the calcined samples.

and reference sample B300-6 were carried out at 550 °C in a fixed-bed reactor with a methanol WHSV of 4 h^{-1}.

As shown in Fig. 10, high-Si hierarchical beta sample B300-1 exhibits an enhanced catalytic activity compared with the reference sample B300-6 synthesized with greater H_2O addition. Specifically, the catalytic lifespan, during which >99% methanol conversion can be kept, is only 6.1 h for the sample B300-6. Comparatively, an obviously prolonged lifetime of 12.2 h could be observed over the hierarchical beta sample B300-1, demonstrating the improved catalytic stability in methanol conversion. Given that the two catalysts have comparable acid densities and sample B300-6 even possesses a little higher amount of T9 Al atoms (Fig. 9), which was demonstrated previously by us to be favorable for the methanol conversion, herein the superior catalytic performance of B300-1 should arise from its unique hierarchical structure. The amounts of coke in the deactivated catalysts are estimated by TG analysis and the results are shown in Fig. 10. A higher coke content (5.4%) is detected on hierarchical sample B300-1, indicating its higher tolerance for coke deposition. The corresponding coke deposition rate calculated for B300-1 (3.0 mg g_{cat}^{-1} h^{-1}) is obviously slower than that for B300-6 (4.9 mg g_{cat}^{-1} h^{-1}), which implies that the hierarchical structure of sample B300-1 can offer better molecular diffusion to depress the successive reactions of coke precursors and their subsequent deposition, and thus prolong the catalytic lifetime.

The product selectivities of the methanol conversion over the samples are shown in Fig. 11. Samples B300-1 and B300-6 display similar evolution trends of product selectivity with propene as the most abundant product, followed by butene and C_{5+}^{N}. The selectivity to propene can reach 55.5% at the beginning of the reaction, which decreases slowly to 50.2% before the occurrence of deactivation (99% methanol conversion). Meanwhile, the selectivity to ethene drops gradually, whereas the selectivity to butene, C_{5+}^{N}, alkanes and aromatics increases as the reaction proceeds. As previous studies have revealed that the methylbenzenes and higher olefins are the active intermediates of aromatic-based cycles and olefin-based cycles, respectively,[31,32,35,42] it is inferred from the higher butene, C_{5+}^{N} and lower aromatic selectivity over both catalysts that the olefin route herein may contribute more to the reaction than the aromatic route. Moreover, differences in product selectivity are also evident between the two catalysts. Hierarchical sample B300-1 gives higher propene, butene and C_{5+}^{N} selectivity than sample B300-6. This should be attributed to the improved molecular diffusion in B300-1, which reduces the probability of secondary reactions of olefin products and is consistent with its lower aromatic and alkane selectivity. The propene/ethene ratio of the samples as a function of TOS was plotted and is shown in Fig. 11. It can be seen that the hierarchical sample presents a higher ratio than B300-6 before the catalyst deactivation, which is desirable for the MTP process due to the reduced energy consumption for the separation of gas products.

The hydrogen transfer index (HTI), which reflects the hydrogen transfer level of the secondary transformation of olefin products, is calculated based on the selectivity ratio of butane to butene. As shown in Fig. 12, the HTI values for sample B300-1 are lower than for sample B300-6. Given the smaller particle sizes, larger external surface area and existence of mesopores for sample B300-1, it is reasonable to see the lower HTI values, which imply faster product diffusion and fewer side reactions, consistent with the longer catalytic

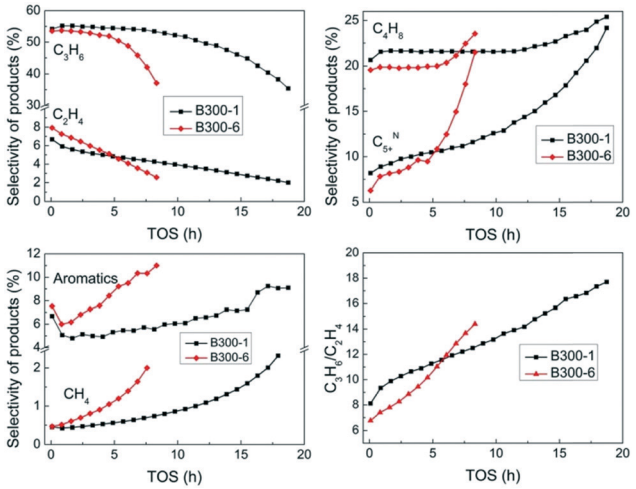

Fig. 11 Product selectivities as a function of TOS over samples B300-1 and B300-6. Reaction conditions: 550 °C, methanol WHSV = 4.0 h^{-1}. C_{1-4}^{0}: C_1–C_4 alkanes; C_{5+}^{N}: non-aromatics with carbon number greater than 4.

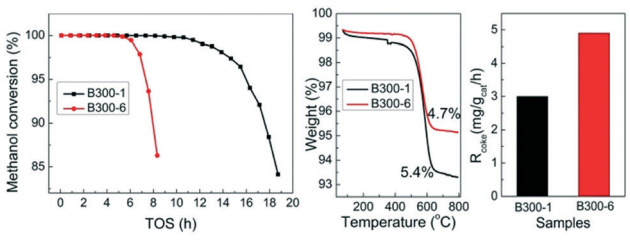

Fig. 10 Methanol conversion as a function of TOS over the high-Si beta zeolites (left) and the corresponding coke content; average coke deposition rate (right). Reaction conditions: 550 °C, methanol WHSV = 4.0 h^{-1}. The coke content was determined by TG analysis based on the weight loss between 300 and 650 °C.

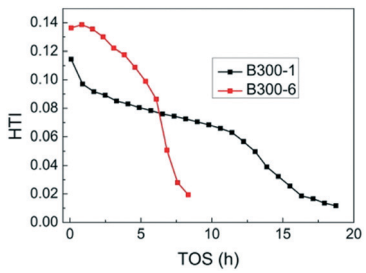

Fig. 12 The hydrogen transfer index ($C_4^{0}/C_4^{=}$) as a function of TOS over samples B300-1 and B300-6. Reaction conditions: 550 °C, methanol WHSV = 4.0 h^{-1}.

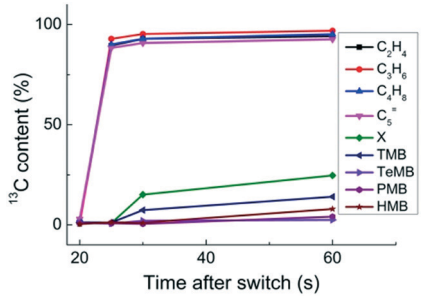

Fig. 13 The ^{13}C content in the effluent olefins and methylbenzenes over high-Si hierarchical beta catalyst. The isotopic switch experiments: continuous flow ^{12}C-methanol conversion for 30 min followed by ^{13}C-methanol feed for 1 min at 550 °C. X: xylene, TMB: trimethylbenzene, TeMB: tetramethylbenzene, PMB: pentamethylbenzene, HMB: hexamethylbenzene.

lifespan and lower selectivity of methane and aromatics. The obviously high selectivity of aromatics on sample B300-6 should be caused by the slower diffusion of olefin products, which further react to form aromatics through oligomerization, cyclization and hydrogen transfer.

The catalytic performance of hierarchical sample B50-1 with a low Si/Al ratio was also investigated under the present reaction conditions (Table S2†). In comparison with the high-Si hierarchical zeolite, the low-Si sample gave distinct product distributions (higher aromatics selectivity) together with a much shorter catalytic lifetime, confirming the importance of the high Si/Al ratio (low acid density) of the catalyst in order to achieve high propene selectivity and long catalytic lifetime.

3.6 ^{12}C/^{13}C-Methanol switch experiment on high-Si hierarchical beta zeolite

The methanol conversion mechanism over high-Si hierarchical beta zeolite was investigated by ^{12}C/^{13}C-methanol isotropic switch experiments. The switch from ^{12}C to ^{13}C-methanol could distinguish the reactivity of organic intermediate species towards ^{13}C-methanol, and the products resulting from the active intermediates contain more ^{13}C atoms.

Fig. 13 displays the ^{13}C contents of the effluent olefins and methylbenzenes after 30 min of ^{12}C-methanol feed followed by ^{13}C-methanol reaction for different times on sample B300-1. Initially, the ^{13}C contents of all products are very low at 20 s after the ^{13}C-methanol switch. Subsequently, the ^{13}C contents in the olefin products (including C_4H_8 and C_5H_{10}) increase sharply at 25 s and then achieve a balance value of above 90% at 30 s, while for the methylbenzenes, the ^{13}C contents increase slowly and the values are less than 20% at 30 s. The distinct difference in the ^{13}C contents of olefin products and aromatic compounds suggests that olefins are much more involved in the reaction of ^{13}C-methanol than the aromatics; the reaction over high-Si hierarchical beta zeolite mainly follows the olefin methylation and cracking mechanism, which contributes to the generation of ethane, propene and higher olefins. This finding is consistent with the low acid density of the high-Si beta catalyst.[35,41,42,54]

4. Conclusions

In summary, we have presented a facile one-pot strategy to fabricate hierarchical high-Si beta zeolite circumventing the addition of mesoporogens by simply lowering the water content in the synthetic gel. The resultant hierarchical particles are single-crystalline in nature and show a nanocrystal-assembled morphology with mesopores rooted in the void space of adjacent nanocrystallites. The water content in the starting gel dictates the crystallization kinetics and consequently the crystal size. The lower water content is prone to promote the formation of nanoaggregates of beta zeolite with an accelerated nucleation and crystal growth rate while inhibiting the fusion of individual nanocrystals into a solid one. The hierarchical high-Si beta zeolite with a low acid density (Si/Al = 277) gave rise to a much longer catalytic lifetime and slower coking rate than the reference sample, showing the advantage of mesoporosity for improving the utilization of acid sites and the molecular transport in the catalyst. Moreover, the appearance of mesopores results in a higher propene selectivity and propene/ethene ratio, which can be explained by the reduced side reactions of olefin products over the hierarchical sample and is consistent with its lower aromatic selectivity and hydration transfer ability. Isotropic switch experiments revealed that the olefin-based cycle was mainly involved in the reaction, leading to the formation of ethene, propene and higher alkenes. This work offers a facile way to synthesize high-Si hierarchical beta and indicates that large-pore zeolites could be excellent MTP catalysts for the achievement of high product Si/Al ratios (low acid densities) and the introduction of mesoporosity.

Conflicts of interest

There are no conflicts to declare.

Acknowledgements

This work was supported by the National Natural Science Foundation of China (21676262) and the Key Research Program of Frontier Sciences, CAS (QYZDB-SSW-JSC040).

Notes and references

1 B. Gao, M. Yang, Y. Qiao, J. Li, X. Xiang, P. Wu, Y. Wei, S. Xu, P. Tian and Z. Liu, *Catal. Sci. Technol.*, 2016, **6**(20), 7569–7578.
2 K. Moeller, B. Yilmaz, R. M. Jacubinas, U. Mueller and T. Bein, *J. Am. Chem. Soc.*, 2011, **133**(14), 5284–5295.
3 E. M. Gallego, C. Paris, M. Rocio Diaz-Rey, M. E. Martinez-Armero, J. Martinez-Triguero, C. Martinez, M. Moliner and A. Corma, *Chem. Sci.*, 2017, **8**, 8138–8149.
4 C. Wang, M. Yang, P. Tian, S. Xu, Y. Yang, D. Wang, Y. Yuan and Z. Liu, *J. Mater. Chem. A*, 2015, **3**(10), 5608–5616.
5 C. Wang, M. Yang, M. Li, S. Xu, Y. Yang, P. Tian and Z. Liu, *Chem. Commun.*, 2016, **52**(38), 6463–6466.
6 Y. Han and F. S. Xiao, *Chin. J. Catal.*, 2003, **24**(2), 149–158.
7 X. Li, M. Sun, J. C. Rooke, L. Chen and B.-L. Su, *Chin. J. Catal.*, 2013, **34**(1), 22–47.

8 D. Verboekend, M. Milina, S. Mitchell and J. Perez-Ramirez, *Cryst. Growth Des.*, 2013, **13**(11), 5025–5035.
9 D. Verboekend and J. Perez-Ramirez, *Catal. Sci. Technol.*, 2011, **1**(6), 879–890.
10 M.-C. Silaghi, C. Chizallet and P. Raybaud, *Microporous Mesoporous Mater.*, 2014, **191**, 82–96.
11 S. Lopez-Orozco, A. Inayat, A. Schwab, T. Selvam and W. Schwieger, *Adv. Mater.*, 2011, **23**(22–23), 2602–2615.
12 E. Koohsaryan and M. Anbia, *Chin. J. Catal.*, 2016, **37**(4), 447–467.
13 K. Zhang, S. Fernandez, S. Kobaslija, T. Pilyugina, J. O'Brien, J. A. Lawrence, , III and M. L. Ostraat, *Ind. Eng. Chem. Res.*, 2016, **55**(31), 8567–8575.
14 K. Egeblad, M. Kustova, S. K. Klitgaard, K. Zhu and C. H. Christensen, *Microporous Mesoporous Mater.*, 2007, **101**(1–2), 214–223.
15 Y. Tong, T. Zhao, F. Li and Y. Wang, *Chem. Mater.*, 2006, **18**(18), 4218–4220.
16 Y. Yuan, P. Tian, M. Yang, D. Fan, L. Wang, S. Xu, C. Wang, D. Wang, Y. Yang and Z. Liu, *RSC Adv.*, 2015, **5**(13), 9852–9860.
17 M. Choi, H. S. Cho, R. Srivastava, C. Venkatesan, D.-H. Choi and R. Ryoo, *Nat. Mater.*, 2006, **5**(9), 718–723.
18 J. Zhu, Y. Zhu, L. Zhu, M. Rigutto, A. van der Made, C. Yang, S. Pan, L. Wang, L. Zhu, Y. Jin, Q. Sun, Q. Wu, X. Meng, D. Zhang, Y. Han, J. Li, Y. Chu, A. Zheng, S. Qiu, X. Zheng and F.-S. Xiao, *J. Am. Chem. Soc.*, 2014, **136**(6), 2503–2510.
19 M. Choi, K. Na, J. Kim, Y. Sakamoto, O. Terasaki and R. Ryoo, *Nature*, 2009, **461**(7261), 246–249.
20 F. N. Gu, F. Wei, J. Y. Yang, N. Lin, W. G. Lin, Y. Wang and J. H. Zhu, *Chem. Mater.*, 2010, **22**(8), 2442–2450.
21 Y. Zhu, Z. Hua, J. Zhou, L. Wang, J. Zhao, Y. Gong, W. Wu, M. Ruan and J. Shi, *Chem. - Eur. J.*, 2011, **17**(51), 14618–14627.
22 F. S. Xiao, L. F. Wang, C. Y. Yin, K. F. Lin, Y. Di, J. X. Li, R. R. Xu, D. S. Su, R. Schlogl, T. Yokoi and T. Tatsumi, *Angew. Chem., Int. Ed.*, 2006, **45**(19), 3090–3093.
23 M. Niwa and N. Katada, *Chem. Rec.*, 2013, **13**(5), 432–455.
24 E. Blomsma, J. A. Martens and P. A. Jacobs, *J. Catal.*, 1996, **159**(2), 323–331.
25 A. Corma, V. Gomez and A. Martinez, *Appl. Catal., A*, 1994, **119**(1), 83–96.
26 J. Song, L. Ren, C. Yin, Y. Ji, Z. Wu, J. Li and F.-S. Xiao, *J. Phys. Chem. C*, 2008, **112**(23), 8609–8613.
27 G. Bellussi, A. Carati, C. Rizzo and R. Millini, *Catal. Sci. Technol.*, 2013, **3**(4), 833–857.
28 Y. S. Tao, H. Kanoh, L. Abrams and K. Kaneko, *Chem. Rev.*, 2006, **106**(3), 896–910.
29 K. Na, M. Choi and R. Ryoo, *Microporous Mesoporous Mater.*, 2013, **166**, 3–19.
30 J. L. Guth, H. Kessler and R. Wey, *Stud. Surf. Sci. Catal.*, 1986, **28**, 121.
31 M. Bjorgen, S. Svelle, F. Joensen, J. Nerlov, S. Kolboe, F. Bonino, L. Palumbo, S. Bordiga and U. Olsbye, *J. Catal.*, 2007, **249**(2), 195–207.
32 P. Tian, Y. Wei, M. Ye and Z. Liu, *ACS Catal.*, 2015, **5**(3), 1922–1938.
33 J. Chen, J. Li, Y. Wei, C. Yuan, B. Li, S. Xu, Y. Zhou, J. Wang, M. Zhang and Z. Liu, *Catal. Commun.*, 2014, **46**, 36–40.
34 J. Chen, J. Li, C. Yuan, S. Xu, Y. Wei, Q. Wang, Y. Zhou, J. Wang, M. Zhang, Y. He, S. Xu and Z. Liu, *Catal. Sci. Technol.*, 2014, **4**(9), 3268–3277.
35 M. Bjorgen, F. Joensen, K.-P. Lillerud, U. Olsbye and S. Svelle, *Catal. Today*, 2009, **142**(1–2), 90–97.
36 J. Li, Y. Wei, J. Chen, S. Xu, P. Tian, X. Yang, B. Li, J. Wang and Z. Liu, *ACS Catal.*, 2015, **5**(2), 661–665.
37 M. Zhang, S. Xu, Y. Wei, J. Li, J. Chen, J. Wang, W. Zhang, S. Gao, X. Li, C. Wang and Z. Liu, *RSC Adv.*, 2016, **6**(98), 95855–95864.
38 W. Zhang, Y. Chu, Y. Wei, X. Yi, S. Xu, J. Huang, M. Zhang, A. Zheng, F. Deng and Z. Liu, *Microporous Mesoporous Mater.*, 2016, **231**, 216–229.
39 O. Mikkelsen and S. Kolboe, *Microporous Mesoporous Mater.*, 1999, **29**(1–2), 173–184.
40 Z. Liu, X. Dong, Y. Zhu, A.-H. Emwas, D. Zhang, Q. Tian and Y. Han, *ACS Catal.*, 2015, **5**(10), 5837–5845.
41 M. Bjorgen, U. Olsbye, D. Petersen and S. Kolboe, *J. Catal.*, 2004, **221**(1), 1–10.
42 M. Zhang, S. Xu, J. Li, Y. Wei, Y. Gong, Y. Chu, A. Zheng, J. Wang, W. Zhang, X. Wu, F. Deng and Z. Liu, *J. Catal.*, 2016, **335**, 47–57.
43 R. Otomo, U. Mueller, M. Feyen, B. Yilmaz, X. Meng, F.-S. Xiao, H. Gies, X. Bao, W. Zhang, D. De Vosh and T. Yokoi, *Catal. Sci. Technol.*, 2016, **6**(3), 713–721.
44 X. Zhao, L. Wang, J. Li, S. Xu, W. Zhang, Y. Wei, X. Guo, P. Tian and Z. Liu, *Catal. Sci. Technol.*, 2017, **7**(4), 5882–5892.
45 J. C. Groen, L. A. A. Peffer and J. Perez-Ramirez, *Microporous Mesoporous Mater.*, 2003, **60**(1–3), 1–17.
46 M. A. Camblor, A. Corma, A. Mifsud, J. PerezPariente and S. Valencia, *Progress in Zeolite and Microporous Materials*, 1997, vol. 105, pp. 341–348.
47 A. Petushkov, G. Merilis and S. C. Larsen, *Microporous Mesoporous Mater.*, 2011, **143**(1), 97–103.
48 D. P. Serrano, R. Van Grieken, P. Sanchez, R. Sanz and L. Rodriguez, *Microporous Mesoporous Mater.*, 2001, **46**(1), 35–46.
49 A. Vjunov, J. L. Fulton, T. Huthwelker, S. Pin, D. Mei, G. K. Schenter, N. Govind, D. M. Camaioni, J. Z. Hu and J. A. Lercher, *J. Am. Chem. Soc.*, 2014, **136**(23), 8296–8306.
50 S. M. Maier, A. Jentys and J. A. Lercher, *J. Phys. Chem. C*, 2011, **115**(16), 8005–8013.
51 A. Janda and A. T. Bell, *J. Am. Chem. Soc.*, 2013, **135**(51), 19193–19207.
52 T. Liang, J. Chen, Z. Qin, J. Li, P. Wang, S. Wang, G. Wang, M. Dong, W. Fan and J. Wang, *ACS Catal.*, 2016, **6**(11), 7311–7325.
53 T. Yokoi, H. Mochizuki, S. Namba, J. N. Kondo and T. Tatsumi, *J. Phys. Chem. C*, 2015, **119**(27), 15303–15315.
54 S. Svelle, U. Olsbye, F. Joensen and M. Bjorgen, *J. Phys. Chem. C*, 2007, **111**(49), 17981–17984.

